ACS Catalysis

Research Article

pubs.acs.org/acscatalysis

Pt Nanoparticles Embedded in Colloidal Crystal Template Derived 3D Ordered Macroporous $Ce_{0.6}Zr_{0.3}Y_{0.1}O_2$: Highly Efficient Catalysts for Methane Combustion

Hamidreza Arandiyan,*[,†,‡] Hongxing Dai,*[,§] Kemeng Ji,[§] Hongyu Sun,[∥] and Junhua Li*[,‡]

[†]Particles and Catalysis Research Group, School of Chemical Engineering, The University of New South Wales, Sydney, New South Wales 2052, Australia

[‡]State Key Joint Laboratory of Environment Simulation and Pollution Control, School of Environment, Tsinghua University, Beijing 100084, People's Republic of China

[§]Key Laboratory of Beijing on Regional Air Pollution Control, Beijing Key Laboratory for Green Catalysis and Separation, Key Laboratory of Advanced Functional Materials, Education Ministry of China, and Laboratory of Catalysis Chemistry and Nanoscience, Department of Chemistry and Chemical Engineering, College of Environmental and Energy Engineering, Beijing University of Technology, Beijing 100124, People's Republic of China

[∥]National Center for Electron Microscopy in Beijing, School of Materials Science and Engineering, The State Key Laboratory of New Ceramics and Fine Processing, Key Laboratory of Advanced Materials (MOE), Tsinghua University, Beijing 100084, People's Republic of China

Supporting Information

ABSTRACT: Three-dimensionally ordered macro/mesoporous $Ce_{0.6}Zr_{0.3}Y_{0.1}O_2$ (3DOM CZY) supported high-dispersion Pt nanoparticles (x wt % Pt/3DOM CZY, x = 0.6, 1.1, and 1.7) were successfully synthesized via the cetyltrimethylammonium bromide/triblock copolymer P123 assisted gas bubbling reduction route. The 3DOM CZY and x wt % Pt/3DOM CZY samples exhibited a high surface area of 84−94 m^2/g. Pt nanoparticles (NPs) with a size of 2.6−4.2 nm were uniformly dispersed on the surface of 3DOM CZY. The 1.1 wt % Pt/3DOM CZY sample showed excellent catalytic performance, giving a $T_{90\%}$ value at 598 °C at gas hourly space velocity (GHSV) of 30000 mL/(g h) and the highest turnover frequency (TOF_{Pt}) of 6.98×10^{-3} $mol/(mol_{Pt}\ s)$ at 400 °C for methane combustion. The apparent activation energy (64 kJ/mol) over 1.1 wt % Pt/3DOM CZY was much lower than that (95 kJ/mol) over Bulk CZY. The effects of water vapor and SO_2 on the catalytic activity of 1.1 wt % Pt/3DOM CZY were also examined. It is concluded that the excellent catalytic activity of 1.1 wt % Pt/3DOM CZY was associated with its high oxygen adspecies concentration, good low-temperature reducibility, and strong interaction between Pt NPs and CZY as well as large surface area and unique nanovoid-walled 3DOM structure.

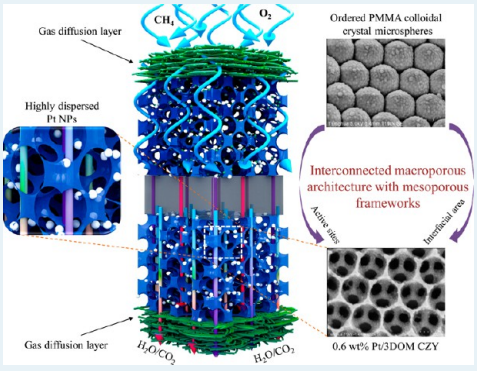

KEYWORDS: *three-dimensionally ordered macropore, mesoporous wall, ceria-zirconia-yttria solid solution, supported Pt nanoparticle, methane combustion*

1. INTRODUCTION

Catalytic combustion of methane is an important technology for energy production and environmental pollution abatement.[1,2] Many materials show an interesting activity, but very few can sustain operation at high temperatures. The thermal stability of combustion catalysts is related to the phase stability of active components and the resistance to the loss of active sites by sintering.[3,4] Ceria is one of the most intensively investigated rare-earth oxides. Among a large number of Ce-based catalysts for methane oxidation, pure ceria exhibits high activity. However, a major drawback of CeO_2 is the serious deactivation due to sintering of particles at high temperatures. It is known that fluorite-type oxides (e.g., nanometer ceria−zirconia solid solutions) have a face-centered-cubic (FCC) crystal structure which has some distinct properties: (i) a large oxygen storage capacity via a facile $Ce^{4+} \Leftrightarrow Ce^{3+}$ redox process, (ii) an ability to promote dispersion of noble metals, (iii) an ability to improve the thermal stability of the support, and (iv) action to promote CH_4 combustion. Many investigations have shown that $Ni/Ce_{0.75}Zr_{0.25}O_2-MgAl_2O_4$, $Ni/Ce_{0.75}Zr_{0.25}O_2-\gamma$-alumina, $CeO_2-Pr_2O_3$, CeO_2-ZrO_2, CeO_2-MnO_x, and nano-Co_3O_4 and CeO_2-CuO were used as active catalysts for the

Received: November 9, 2014
Revised: February 7, 2015
Published: February 9, 2015

DOI: 10.1021/cs501773h
ACS Catal. 2015, 5, 1781−1793

oxidation of carbon monoxide, methane, soot, and NO_x.[5−9] Among these binary compounds, $Ce_{1-x}Zr_xO_2$ (x = 0.1−0.9) shows good thermal stability and redox behaviors.[10] The content of doped ZrO_2 should not exceed 50% for optimum performance.[11] According to Madier et al.,[12] $Ce_{0.63}Zr_{0.37}O_2$ exhibited promising properties with the largest oxygen storage capacity and the highest reactivity in O_2 exchange. In the past years, our group have focused on the partial replacement of Ce by trivalent rare-earth-metal ions (e.g., Y^{3+}) that could promote the formation of oxygen vacancies and noticeably improve the thermal stability, redox ability, and oxygen storage capacity (OSC) of the solid solutions,[13−15] hence enhancing catalytic performance.[15] In addition, the incorporation of Y^{3+} could facilitate the diffusion of lattice oxygen by creating anion defects and thus decrease the reduction temperature of the solid solutions.[14,15] Usually, complex oxides can be synthesized by means of the methods and different precursors, such as alkoxides,[16] molten salts,[17] sol−gel,[18] and thermal decomposition.[19] In the sol−gel method, reactants are dissolved in a suitable solvent (e.g., water). An intermediate product is interacted with citric[20] or pluronic P123,[21] which usually leads to difficult preservation of pore structures and hence to a low surface area. Therefore, a novel strategy is highly desired to prepare porous complex oxide materials with high surface areas.

Recently, this problem has been solved by the colloidal crystal-templating method that can create three-dimensionally ordered macropores (3DOM) due to its several advantages: (i) a single-step low-temperature process, (ii) facile control in composition and morphology, and (iii) wide suitability for metal precursors. For example, by using monodispersed polystyrene (PS) beads as a template, Sadakane et al.[22] fabricated 3DOM-structured $La_{1-x}Sr_xFeO_3$ (x = 0−0.4) with a surface area of 24−49 m^2/g. With PS beads as a template, Hara et al.[23] obtained 3DOM-structured $Li_{0.35}La_{0.55}TiO_3$. Using poly(methyl methacrylate) (PMMA) as a template, 3DOM-structured Pt/TMO (TMO = Mn, Fe, Co, Ni, Cu) with a surface area of 36−40 m^2/g,[24] 3DOM-structured xAuPd/3DOMCo_3O_4 (x = 0.50−1.99) with a surface area of 33−36 m^2/g,[25] and 3DOM-structured $Au_{0.04}/Ce_{0.8}Zr_{0.2}O_2$[26] could be generated. To the best of our knowledge, however, there have been no reports on the successful preparation of Pt nanoparticles (NPs) supported on 3D ordered macroporous $Ce_{0.6}Zr_{0.3}Y_{0.1}O_2$ with formation of highly crystalline mesoporous walls and their catalytic applications for the combustion of methane. In the past several years, our group has investigated the fabrication, characterization, and physicochemical properties of 3DOM-structured materials with high surface areas by surfactant-assisted PMMA-templating approaches, such as Co_3O_4/3DOM $La_{0.6}Sr_{0.4}CoO_3$ (surface area 29−32 m^2/g),[27] CrO_x/3DOM $InVO_4$ (surface area 41.3−52.3 m^2/g),[28] 3DOM $InVO_4$ (surface area 35−52 m^2/g),[29] Au/3DOM Mn_2O_3 (surface area 34−38 m^2/g),[30] Au/3DOM $LaCoO_3$ (surface area 24−29 m^2/g),[31] and Au/3DOM $La_{0.6}Sr_{0.4}MnO_3$ (surface area 31−33 m^2/g).[32] We observed that some of the 3DOM materials showed excellent catalytic performance in the combustion of toluene and methane.[33−35]

Herein, we report for the first time the facile dual-template preparation of Pt NPs supported on 3DOM-structured $Ce_{0.6}Zr_{0.3}Y_{0.1}O_2$ (3DOM CZY) with nanovoid-like or mesoporous skeletons (x wt % Pt/3DOM CZY; x = 0, 0.6, 1.1, 1.7), which was based on the use of a cetyltrimethylammonium bromide (CTAB) assisted gas bubbling reduction route with H_2PtCl_6/$NaBH_4$ and amphiphilic triblock copolymer (Pluronic P123, MW_{av} = 5800 g/mol) as a soft template and well-arrayed colloidal crystal PMMA microspheres as a hard template to generate a 3DOM structure (Figures S1 and S3 in the Supporting Information). It was found that the obtained x wt % Pt/3DOM CZY catalysts have great utility because of their unique properties, such as high surface area, controllable composition, crystallinity, thermal and chemical stability, high porosity, and narrow pore size distribution as well as their excellent catalytic performance for CH_4 combustion.

2. EXPERIMENTAL SECTION

2.1. Synthesis of Monodisperse PMMA Microspheres. Monodisperse PMMA microspheres with an average diameter of ca. 300 nm (Figure S1 in the Supporting Information) were synthesized by adopting the procedures described in the literature.[35,36] A solution of 0.40 g (3.00 mmol) of potassium peroxydisulfate ($K_2S_2O_8$) in 1500 mL of deionized water was mixed with stirring at 400 rpm, heated to 70 °C, and degassed with flowing N_2 in a separable four-neck 2000 mL round-bottom flask. After the solution was equilibrated at 70 °C, 115 mL of methyl methacrylate was poured into the flask, and the resulting suspension was stirred at 70 °C for 60 min. The PMMA colloidal crystal template was prepared with 120 mL of the colloidal suspension (ca. 10.0 g) in a 25 mL centrifugation tube for 75 min. The supernatant was removed and the precipitate was washed three times using deionized water for the total removal of $K_2S_2O_8$. When the deionized water was evaporated in a water bath at 80 °C, the obtained wet solid was first dried at room temperature for 48 h and then ground well. During the polymerization, several factors (such as initiators, monomer, temperature, and the stirring rate) could influence the sizes of the PMMA microspheres.

2.2. Synthesis of 3DOM $Ce_{0.6}Zr_{0.3}Y_{0.1}O_2$ Solid Solutions. The 3DOM CZY support was fabricated by adopting a cetyltrimethylammonium bromide (CTAB) assisted method. With magnetic stirring at room temperature, stoichiometric amounts of $Ce(NO_3)_3{\cdot}6H_2O$ (6.00 mmol), $ZrO(NO_3)_2{\cdot}2H_2O$ (3.00 mmol), and $Y(NO_3)_3{\cdot}6H_2O$ (1.00 mmol) were first dissolved in 5 mL of deionized water; the mixed solution was then added to the surfactant-containing solution (20.0 mmol of CTAB + 75.0 mL of deionized water). After being well mixed, 200 mmol of urea was finally added dropwise to the above mixed solution with stirring for 2 h and the pH was carefully regulated to 11 for the generation of yellowish coprecipitates. The CZY/CTAB/urea molar ratio was 1/2/20. After being filtered and washed three times with deionized water and methanol, ca. 3.00 g of highly ordered PMMA colloidal crystal microspheres was then added and soaked with the above mixed solution. After the PMMA microspheres were thoroughly wetted, the excess liquid was filtered via a Buchner funnel connected to −0.07 MPa vacuum (Figure S1 in the Supporting Information). Finally, after filtration and drying at room temperature for 24 h, the solid was transferred to a ceramic boat and thermally treated in a tubular furnace first in a N_2 flow of 50 mL/min at a ramp of 1 °C/min from room temperature to 300 °C for 3 h and then cooled under the same atmosphere to room temperature and finally treated in an air flow of 50 mL/min at a ramp of 1 °C/min from room temperature to 800 °C and kept at this temperature for 4 h, thus generating the 3DOM CZY catalyst.

2.3. Synthesis of x wt % Pt/3DOM $Ce_{0.6}Zr_{0.3}Y_{0.1}O_2$ Catalysts. The CZY-supported platinum (x wt % Pt/3DOM CZY) catalysts were prepared via a gas-bubbling CTAB/P123-

DOI: 10.1021/cs501773h
ACS Catal. 2015, 5, 1781−1793

Scheme 1. Schematic Illustration of Loading Pt NPs on 3DOM CZY Catalysts

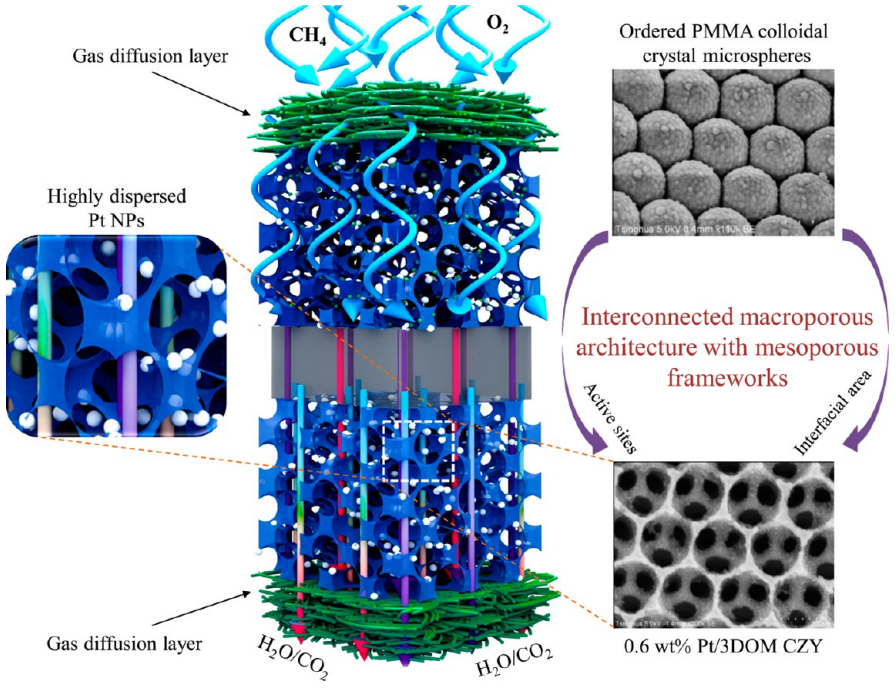

protected reduction method. The typical preparation procedure is as follows: the amount of CTAB (3.00 mL) in the presence of Pluronic P123 (1.20 g) was added to a 100 mg/L H_2PtCl_6 aqueous solution (Pt/CTAB mass ratio 1.5/1) at room temperature under vigorous gas bubbling for 10 min. After rapid injection of an aqueous solution of 0.1 mol/L $NaBH_4$ ($Pt/NaBH_4$ molar ratio 1/5) a dark brown platinum sol was obtained. A desired amount (theoretical Pt loading 0.5, 1.0, or 1.5 wt %) of the 3DOM CZY support was then added to the platinum sol, and the obtained suspension was subjected to sonication (60 kHz) for 30 s. A gas-bubble-assisted stirring operation with three bubble outlets in solution was used to further agitate the system, and the suspension was vigorously bubbled with N_2 for 6 h. The solid was filtered and washed with deionized water until no chloride ions were detected using a 0.1 mol/L $AgNO_3$ aqueous solution. After being dried in an oven at 60 °C for 24 h and calcined in an O_2 flow of 30 mL/min at 500 °C for 1 h, the obtained 3DOM CZY-supported platinum samples were denoted as *x* wt % Pt/3DOM CZY, as illustrated in Scheme 1. The results of inductively coupled plasma atomic emission spectroscopic (ICP-AES) investigations reveal that the real Pt loading (*x*) was 0.6, 1.1, and 1.7 (Table S1 in the Supporting Information), respectively.

2.4. Synthesis of Conventional Nonporous Bulk Sample $Ce_{0.6}Zr_{0.3}Y_{0.1}O_2$. The conventional nonporous bulk $Ce_{0.6}Zr_{0.3}Y_{0.1}O_2$ (denoted as Bulk CZY) and 1.2 wt % Pt/Bulk CZY catalysts were prepared via the sol–gel complexing route[35] and gas-bubbling CTAB/P123-protected reduction method,[32] respectively, and the catalyst precursors were calcined in air at 850 °C for 4 h. For the sake of better presentation, the main preparation conditions of the CZY materials are summarized in Table S1 in the Supporting Information.

2.5. Catalyst Characterization. All of the as-prepared samples were characterized by means of inductively coupled plasma atomic emission spectroscopy (ICP-AES), X-ray diffraction (XRD), high-resolution scanning electron microscopy (HRSEM), high resolution transmission electron microscopy (HRTEM), selected-area electron diffraction (SAED), N_2 adsorption–desorption (Brunauer–Emmett–Teller, BET), H_2 temperature-programmed reduction (H_2-TPR), and X-ray photoelectron spectroscopy (XPS). The detailed procedures are described in the Supporting Information.

2.6. Catalytic Activity Measurement. Catalytic activity evaluation was conducted in a fixed-bed quartz tubular microreactor (i.d. = 6.0 mm), as shown in Figure S2 in the Supporting Information. To minimize the effect of hot spots, the sample (20 mg, 40–60 mesh) was diluted with 0.25 g of quartz sand (40–60 mesh). The volumetric composition of the reactant mixture was 2 vol % CH_4 + 20 vol % O_2 + 78 vol % N_2 (balance), and the total flow was 41.6 mL/min, thus giving a gas hourly space velocity (GHSV) of ca. 30000 mL/(g h)). The concentrations of the reactants and products were monitored online by a gas chromatograph (Agilent 7890A) equipped with FID and TCD detectors using Porapack-Q/molecular sieve 5A and RT-QPlot divinylbenzene PLOT columns, respectively. The balance of carbon throughout the investigations was estimated to be 99.5%. The relative errors for the gas concentration measurements were less than ±1.5%. Catalytic activities of the samples were evaluated using the temperatures ($T_{10\%}$, $T_{50\%}$, and $T_{90\%}$) required for methane conversions of 10, 50, and 90%, respectively. CH_4 conversion was defined as $(c_{inlet} - c_{outlet})/c_{inlet} \times 100\%$, where c_{inlet} and c_{outlet} are the inlet and outlet CH_4 concentrations, respectively.

3. RESULTS AND DISCUSSION

3.1. Crystal Phase Composition. To confirm the formation and phase structures of the *x* wt % Pt/3DOM CZY samples, XRD measurements were conducted using a Philips PW-1800 diffractometer with Cu Kα radiation, and the results are illustrated in Figure 1. All of the diffraction peaks of the *x* wt % Pt/3DOM CZY samples could be indexed to (111), (200), (220), (311), (222), (400), and (331) lattice planes, and the CZY in *x* wt % Pt/3DOM CZY possessed a fluorite-type

DOI: 10.1021/cs501773h
ACS Catal. 2015, 5, 1781–1793

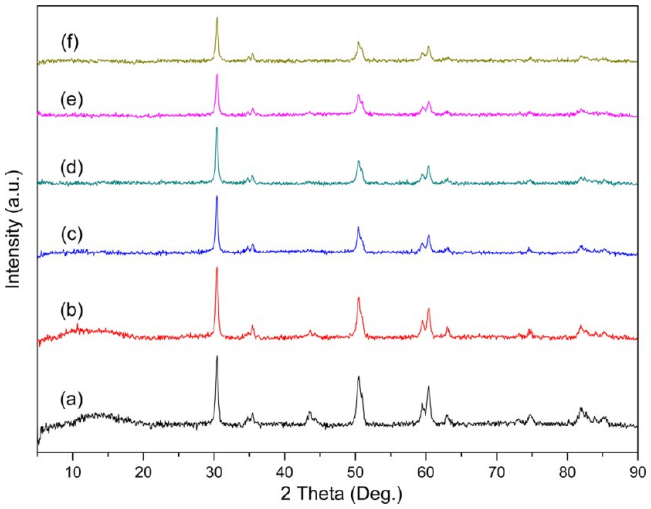

Figure 1. XRD patterns of fresh (a) Bulk CZY, (b) 3DOM CZY, (c) 1.2 wt % Pt/Bulk CZY, (d) 0.6 wt % Pt/3DOM CZY, (e) 1.1 wt % Pt/3DOM CZY, and (f) 1.7 wt % Pt/3DOM CZY catalyst.

structure of CeO_2 with a face-centered-cubic (FCC) lattice. The XRD patterns of the 3DOM CZY and *x* wt % Pt/3DOM CZY samples displayed a broadening feature, implying formation of small CZY crystallites. The crystal phases of Pt NPs were not detected, indicating the high dispersion and small sizes of Pt NPs on the surface of 3DOM CZY. The average crystallite sizes estimated by the Scherrer equation of 3DOM CZY and 1.1 wt % Pt/3DOM CZY were about 41.3 and 41.7 nm, respectively, as given in Table 1. The XRD patterns (not shown here) of the *x* wt % Pt/3DOM CZY sample after H_2-TPR were rather similar to those of the corresponding fresh samples. Meanwhile, no obvious changes in crystallite size were observed after Pt NP deposition on the surface of 3DOM CZY. Therefore, it can be concluded that the deposition of Pt NPs on the surface of 3DOM CZY had no significant impact on the crystal phase, crystallite size, and crystallinity of 3DOM CZY.

Table 1. BET Surface Areas, Pore Volumes, CZY Crystallite Sizes (D_{CZY}), Pt Particle Sizes, and Real Pt Content of the CZY and *x* wt % Pt/3DOM CZY Samples

sample	BET surface area (m^2/g)	pore volume (cm^3/g)	D_{CZY} (nm)[a]	Pt particle size (nm)[b]	Pt content (wt %)[c]
3DOM CZY	94	0.11	41.3		
0.6 wt % Pt/3DOM CZY	95	0.12	42.5	2−5	0.6
1.1 wt % Pt/3DOM CZY	84	0.12	41.7	2−5	1.1
1.7 wt % Pt/3DOM CZY	87	0.11	41.2	2−5	1.7
Bulk CZY	69	0.014	156.2		
1.2 wt % Pt/Bulk CZY	71		155.7	3−8	1.2

[a]Data determined on the basis of the XRD results according to the Scherrer equation using the fwhm of the (110) line of CZY. [b]Estimated according to the TEM images. [c]Determined by the ICP-AES technique.

3.2. Result of SEM. Shown in Figure 2 as well as Figures S3−S7 in the Supporting Information are the representative SEM and HRSEM images of the PMMA, 3DOM CZY, *x* wt % Pt/3DOM CZY, and Bulk CZY samples. It is clear that all of the samples obtained after calcination at 800 °C exhibited 3DOM architectures (Figure 2b−k) of different quality. Figure 2a and Figure S3 show the SEM images of PMMA monodisperse microspheres. It can be seen that the synthesized microspheres had good monodispersity and did not adhere to each other. Moreover, from Figures S3−S7 it can be seen that the colloidal crystal PMMA templates formed a face-centered-cubic close-packed structure. Meanwhile, Figure 2d−k shows the HRSEM images of the 3DOM CZY and *x* wt % Pt/3DOM CZY samples with different Pt loadings. Highly ordered macroporous structures could be obtained via the long-range replication of the 3D close-packed PMMA template.[35,36] It is known that the soft (CTAB/P123) templates and hard polymer templates (PMMA) can support the conversion of the metal precursor(s) to a solid-state porous framework at lower temperatures. From the HRSEM images of the 3DOM CZY and *x* wt % Pt/3DOM CZY samples (Figure 2c,f,i,k and Figures S4−S7), the next layer of the macroporous structure was clearly visible and the containing periodic voids were interconnected through the open windows: 121−147 nm in diameter (Figure 2f) and a wall thickness of 13−19 nm, which corresponded to a shrinkage of 20−30% in comparison with the initial size (ca. 300 nm) of PMMA microspheres. The 3DOM CZY sample showed a high-quality 3DOM structure (Figure 2b,c and Figure S4). After Pt NPs loading, the obtained 0.6 wt % Pt/3DOM CZY sample (Figures 2d−f and Figure S5) displayed a better quality of 3DOM architecture than the 3DOM CZY sample (Figure 2b,c), giving rise to surface areas of the former sample higher than that of the latter one. However, with increasing Pt NPs loading to 1.1 wt %, the size of the open window decreased (Figures 2g−i and Figure S6). This indicates that the Pt NPs were deposited on the surface of 3DOM CZY, and an excess Pt NPs loading (e.g., 1.7 wt % Pt/3DOM CZY) could not affect the diffusion of reactants in the macroporous materials (Figure 2j,k and Figure S7). The Bulk CZY sample was composed of irregularly morphological particles with a

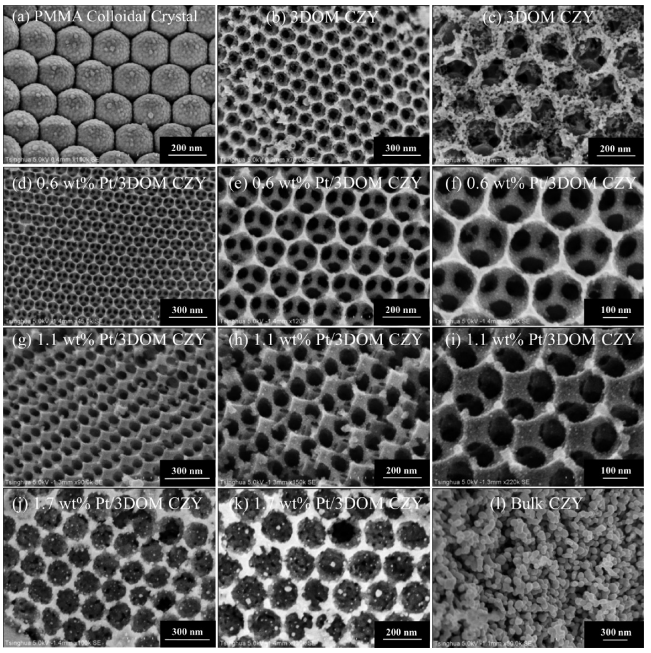

Figure 2. HRSEM images of the 3DOM CZY support and *x* wt % Pt/3DOM CZY and Bulk CZY catalysts.

DOI: 10.1021/cs501773h
ACS Catal. 2015, 5, 1781−1793

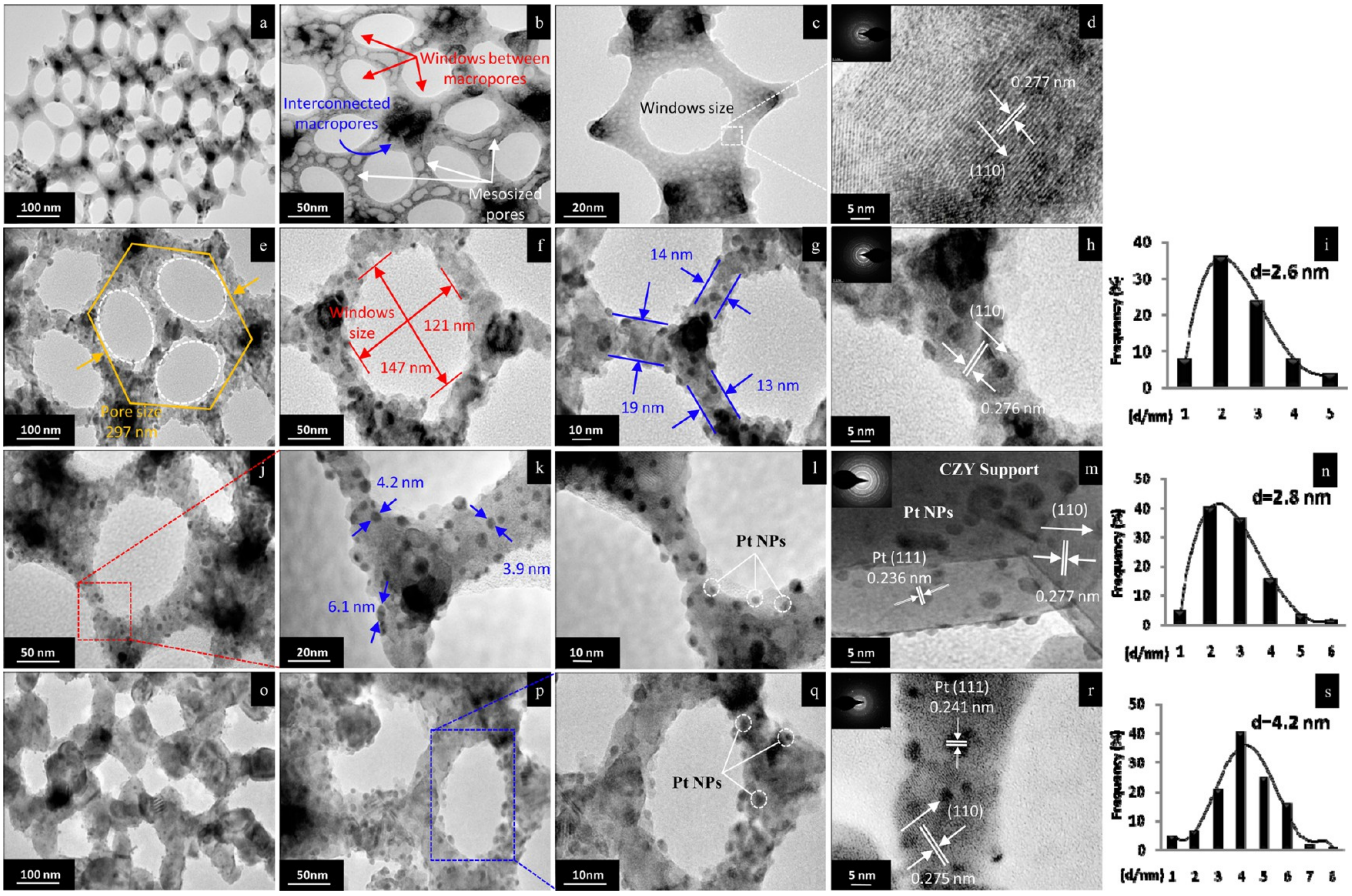

Figure 3. TEM and high-resolution TEM images as well as the SAED patterns (insets) of (a–d) 3DOM CZY support, (e–i) 0.6 wt % Pt/3DOM CZY, (j–n) 1.1 wt % Pt/3DOM CZY, and (o–s) 1.7 wt % Pt/3DOM CZY.

length of 0.5–1.0 μm (Figure 2l). The 3D close-packed PMMA template and the CTAB/P123 surfactant played a key role in the fabrication of 3DOM-structured materials. The glassy transition temperature of the PMMA template was ca. 370 °C in air,[22,35,36] close to the decomposition temperature of cerium(III) nitrate hydrate. During the calcination process in N_2 at 300 °C, the partial carbonization of PMMA took place (as shown in Scheme 1) and the generated amorphous carbon would act as a hard template to guarantee the formation of high-quality 3DOM-structured CZY before the completely oxidative removal of the PMMA template at 800 °C.[36] The small and well-dispersed Pt NPs might interact more strongly with CH_4 and would show higher CH_4 oxidation activities than their corresponding large particles and bulk entities.

3.3. Result of TEM. Figure 3 shows the TEM and HRTEM images and size distributions as well as the SAED patterns of the 3DOM CZY and *x* wt % Pt/3DOM CZY samples. The TEM images reveal that 3DOM CZY and *x* wt % Pt/3DOM CZY possessed a well-defined interconnected macroporous structure with two-dimensional aligned mesopore size of 3.5–4.6 nm, an interconnected macropore wall thickness of 13–19 nm, and a mean Pt particle size of 2.6–4.2 nm (Figure 3a–c,e), which was also proven by the SEM observations (Figure 2f,i,k and Figures S4–S7 in the Supporting Information). After Pt NPs were loaded on the 3DOM CZY support, the resulting 0.6 wt % Pt/3DOM CZY, 1.1 wt % Pt/3DOM CZY, and 1.7 wt % Pt/3DOM CZY samples maintained morphological and structural features similar to those of the 3DOM CZY support (Figure 3e–h,j–m,o–r). The magnified HRTEM image suggests that a mesoporous structure exists in the macroporous skeletons of the CZY support due to the aggregation of CZY (Figure 3d), which was further confirmed by BJH pore size distributions. The existence of a macro-/mesoporous structure in *x* wt % Pt/3DOM CZY was also greatly beneficial for the transfer of reactants and products, which would favor the improvement in catalytic performance. From the HRTEM images of the 3DOM CZY and *x* wt % Pt/3DOM CZY samples, the lattice spacings (*d* values) of the (110) crystal plane of 3DOM CZY and *x* wt % Pt/3DOM CZY were estimated to be 0.275–0.277 nm (Figure 3d,h,m,r), rather close to that of the standard $Ce_{0.75}Zr_{0.25}O_2$ sample (JCPDS PDF 28-0271). Furthermore, well-resolved lattice fringes of the exposed Pt (111) crystal plane in the Pt/3DOM CZY samples (Figure 3h,m,r) were recorded, and the *d* value (0.235–0.241 nm) of the Pt (111) crystal plane was not far away from that (0.24 nm) of the standard Pt sample (JCPDS PDF 01-1194). After loading Pt NPs, one can also observe from Figure 3g,k,l,q that the Pt^0 NPs were homogeneously dispersed on the surface of 3DOM CZY. The size distributions of Pt NPs in *x* wt % Pt/3DOM CZY were in the range 2–8 nm (Table 1). After statistical analysis of the sizes of more than 200 Pt NPs in the HRTEM images, one can see that mean diameters of Pt NPs in the 0.6 wt % Pt/3DOM CZY, 1.1 wt % Pt/3DOM CZY, and 1.7 wt % Pt/3DOM CZY samples were 2.6, 2.8, and 4.2 nm (Figure 3i,n,s), respectively. This result is in good agreement with that revealed by the XRD investigations (Figure 1 and Table 1). It is quite clear that the Pt NPs in 1.1 wt % Pt/3DOM CZY were smaller in size and more uniform in comparison to those in 1.7

DOI: 10.1021/cs501773h
ACS Catal. 2015, 5, 1781–1793

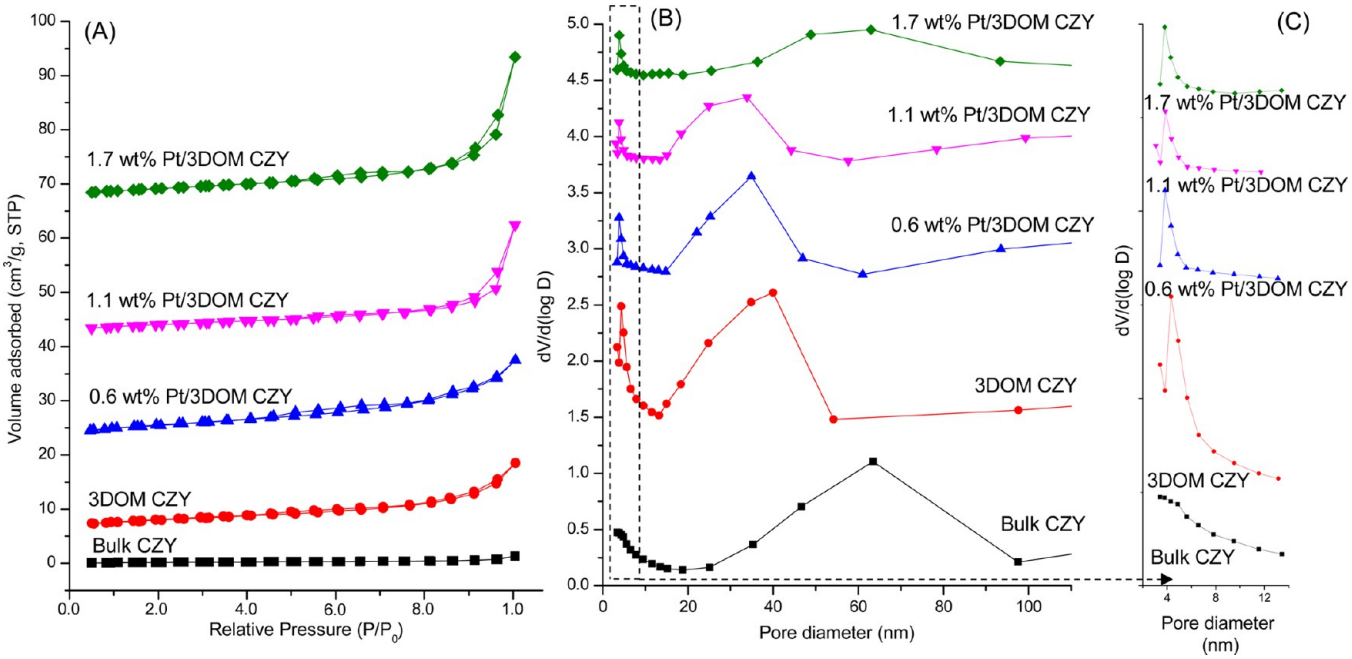

Figure 4. (A) Nitrogen adsorption−desorption isotherms and (B, C) pore-size distributions of 3DOM CZY support, *x* wt % Pt/3DOM CZY, and Bulk CZY catalysts.

wt % Pt/3DOM CZY. This suggests that the interface interaction between 3DOM CZY and Pt NPs take place at the atomic level, which was possibly due to the partial incorporation of oxidized Pt species into the bulk structure of the support.[24,26,38] It is an indication of existence of strong metal−support interactions (SMSIs). The interaction between Pt NPs and 3DOM CZY would be favorable for the mobility of lattice oxygen and might be conducive to the production of oxygen vacancies on the surface of the *x* wt % Pt/3DOM CZY samples. The recording of multiple bright electron diffraction rings in the SAED patterns of the 3DOM CZY and *x* wt % Pt/3DOM CZY samples (insets of Figure 3h,m,r) suggests that the aforementioned samples were polycrystalline. Additional TEM images of the 3DOM CZY, 0.6 wt % Pt/3DOM CZY, 1.1 wt % Pt/3DOM CZY, and 1.7 wt % Pt/3DOM CZY samples with nanovoids on the macroporous walls are shown in Figures S8 and S9 om the Supporting Information. During the preparation of *x* wt % Pt/3DOM CZY, CTAB would function as a multifunctional reagent for the formation of 3DOM architecture with excellent chemical and thermal stability. The CTAB/P123-mediated route not only produced a high-quality 3DOM structure but also stabilized it against conglomeration. Thus, the precipitation reagent had an important effect on the quality of the 3DOM structure and the particle size of Pt NPs in *x* wt % Pt/3DOM CZY.

3.4. Pore Structure and Surface Area. The porous structures of the 3DOM CZY and *x* wt % Pt/3DOM CZY samples were further substantiated by the N_2 adsorption−desorption isotherms (Figure 4A). Each of the samples displayed a type IV isotherm with a type H3 hysteresis loop in the relative pressure (p/p_0) range of 0.9−1.0. The hysteresis loops in the low and high relative pressure ranges of the Pt-loaded samples were slightly different from that of the 3DOM CZY support, indicative of the discrepancy in pore size distribution (Figure 4B,C). The appearance of a small H2-type hysteresis loop in the p/p_0 range of 0.2−0.9 of each sample was an indication of mesoporous formation.[29,31,35] Meanwhile, the low-pressure portion of the almost linear middle section of the isotherm could be attributed to the unrestricted mono-/multilayer adsorption, suggesting that the samples possessed macroporous structures.[39] Such a deduction was confirmed by the pore size distributions (Figure 4B) of these samples. The 1.7 wt % Pt/3DOM CZY and Bulk CZY samples displayed broad pore size distributions centered at ca. 63 and 64 nm (Figure 4B), respectively.

The BET surface areas of the *x* wt % Pt/3DOM CZY samples were in the range 84−95 m^2/g, higher than those (69 and 71 m^2/g) of the nonporous Bulk CZY and 1.2 wt % Pt/Bulk CZY samples. The surface area decreased with a rise in Pt NP loading from *x* = 0.6 to 1.1 wt % but increased to 87 m^2/g at *x* = 1.7 wt %. The 1.1 wt % Pt/3DOM CZY sample possessed a large surface area (84 m^2/g) due to the thinner walls and the presence of nanovoids. Moreover, the surface area (84 m^2/g) of 1.1 wt % Pt/3DOM CZY calcined at 800 °C was markedly higher than that (23−30 m^2/g) of 3DOM $LaFeO_3$,[22] that (29.8−32.7 m^2/g) of Au/3DOM $LaMnO_3$,[30] and that (24−29 m^2/g) of Au/3DOM $LaCoO_3$.[31] From Table 1, one can see that the presence of mesopores in the skeletons of macropores in the *x* wt % Pt/3DOM CZY samples contributed significantly to the enhancement in surface area.[29,35,36] In addition, the pore volumes of the 3DOM-structured samples were approximately equal (0.11−0.12 cm^3/g), much larger than that (0.014 cm^3/g) of the nonporous Bulk CZY sample (Table 1). Hence, in comparison to the Bulk CZY sample, the *x* wt % Pt/3DOM CZY samples with mesopores in the skeletons of macropores possessed higher surface areas, which could provide more active sites, and the highly developed pore structure could facilitate the adsorption and diffusion of reactant molecules.[37] Therefore, such unique properties would be beneficial for the enhancement in catalytic activity of a solid sample.

3.5. Surface Composition, Metal Oxidation State, and Oxygen Species. X-ray photoelectron spectroscopy (XPS) is an effective technique to investigate the surface element compositions, metal oxidation states, and adsorbed species of

DOI: 10.1021/cs501773h
ACS Catal. 2015, 5, 1781−1793

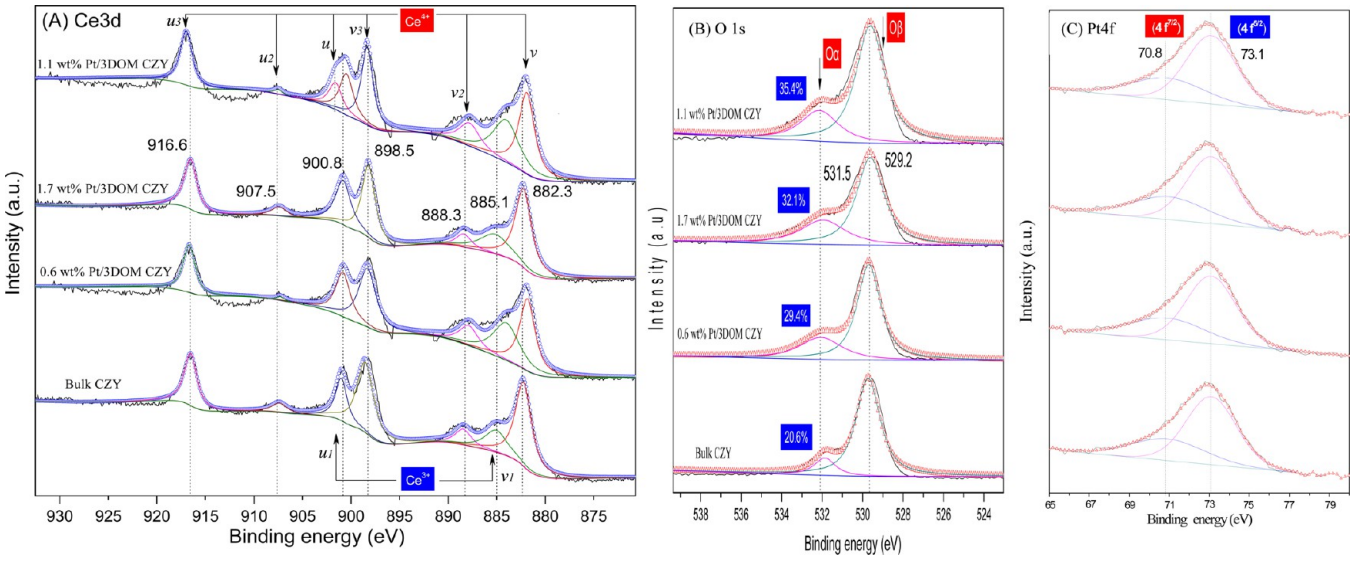

Figure 5. (A) Ce 3d, (B) O 1s, and (C) Pt 4f XPS spectra of *x* wt % Pt/3DOM CZY and Bulk CZY catalysts.

Table 2. Surface Element Compositions and H_2 Consumption of the CZY and *x* wt % Pt/3DOM CZY Samples

	molar ratio				methane combustion (°C)		
sample	Ce^{4+}/Ce^{3+}	$Pt^{\delta+}/Pt^0$	$O_\alpha/(O_\alpha + O_\beta)$	H_2 consumption (mmol/G)[a]	$T_{10\%}$	$T_{50\%}$	$T_{90\%}$
3DOM CZY	1.46		24.7	15.8	352	590	511
0.6 wt % Pt/3DOM CZY	1.25	0.39	29.4	14.5	363	489	543
1.1 wt % Pt/3DOM CZY	1.12	0.46	35.4	14.1	385	434	598
1.7 wt % Pt/3DOM CZY	1.08	0. 52	32.1	13.7	437	462	663
Bulk CZY	0.69		20.6	18.0	476	671	698
1.2 wt % Pt/Bulk CZY	0.58	0.41	28.5	15.8	562	558	750
used 1.1 wt % Pt/CZY[b]					389	440	607

[a]The data were estimated by quantitatively analyzing the H_2 TPR profiles. [b]The 1.1 wt % Pt/3DOM CZY sample after 32 h of on-stream reaction for CH_4 oxidation under the conditions of GHSV = 30000 mL/(g h), 2% CH_4 + 20% O_2 + 78% N_2 (balance), and total flow 41.6 mL/min.

a solid sample. Figure 5 shows the Ce 3d, O 1s, and Pt 4f XPS spectra of the Bulk CZY and *x* wt % Pt/3DOM CZY samples. From Figure 5A, one can observe that there were two sets of signals: one was sub-bands (labeled *u* and *v*) corresponding to the $3d_{3/2}$ and $3d_{5/2}$ contributions, where *u1* and *v1* represent the $3d_{10}4f_1$ initial electronic state corresponding to Ce^{3+}, and the other was *u, u2, u3, v, v2,* and *v3* corresponding to the $3d_{10}4f_0$ state of Ce^{4+}.[39−41] The signals at 885.1 eV (*v1*) and 900.8 eV (*u1*) could be assigned to unique photoelectrons corresponding to Ce^{3+} state and the signal at 907.5 eV (*u2*) could be assigned to Ce^{4+} according to the literature.[40−42] That is to say, the cerium in our CZY samples existed in tri- and tetravalent states. Similar scenarios also occurred in the CeO_2,[43] $Ce_{1-x}Zr_xO_2$,[44] and $RE_{0.6}Zr_{0.3-x}Y_xO_2$[45] samples. According to the XPS spectra, we calculated the surface compositions of the samples, as shown in Table 2. For these samples, the surface $O_\alpha/(O_\alpha + O_\beta)$ and Ce^{3+}/Ce^{4+} atomic ratios increased in the same sequence. It is well-known that $Ce_{1-x}Zr_xO_2$ materials have good oxygen storage/release ability due to the presence of cerium ions with mixed oxidation states,[43,44] which would facilitate the redox process $Ce^{3+} \Leftrightarrow Ce^{4+}$.[45] As shown in Figure S10 in the Supporting Information, the signal due to the surface carbonate species was rather weak, indicating that there was only a trace amount of surface carbonate species on the surface of the samples. As for the O 1s XPS spectra of the samples (Figure 5B), there was an asymmetrical peak at BE = ca. 530 eV, which could be decomposed into two components at BE = 529.2 and 531.5 eV. The sub-bands at lower binding energy (529.2−530.3 eV) could be assigned to the lattice oxygen O^{2-} (hereafter denoted as O_β), and the sub-bands at higher binding energy (531.5−532.3 eV) corresponded to the surface chemisorbed oxygen (hereafter denoted as O_α) species[45] in/on the samples. The relative ratio of O_α calculated by $O_\alpha/(O_\alpha + O_\beta)$ on 1.1 wt % Pt/3DOM CZY (35.4%), 1.7 wt % Pt/3DOM CZY (32.1%), and 0.6 wt % Pt/3DOM CZY (29.4%) were higher than those on Bulk CZY (20.6%), 1.2 wt % Pt/Bulk CZY (28.5), and 3DOM CZY (24.7). This result suggests that the synergistic effect between Pt and Ce species could facilitate formation of more surface oxygen concentrations (Figure 5B). It has been reported that there was the presence of oxygen vacancies in $Ce_{1-x}Zr_xO_2$[46] and the doping of Y^{3+} to the lattice of ceria−zirconia solid solution could further increase the density of oxygen vacancies.[45] Meanwhile, since O_α is more active than O_β due to the higher mobility of the former, the higher relative ratio of O_α on *x* wt % Pt/3DOM CZY would be favorable for CH_4 oxidation and thus enhance the catalytic activity at low temperatures.

The Pt 4f core level spectra of the Bulk CZY and *x* wt % Pt/3DOM CZY samples are shown in Figure 5C, in which distinct peaks appeared at binding energies of 70.8 and 73.1 eV, attributable to Pt $4f_{7/2}$ and Pt $4f_{5/2}$, respectively. The components at binding energies of 70.8 and 73.1 eV were assigned to the Pt^0 and $Pt^{\delta+}$ species, respectively. The $Pt^{\delta+}/Pt^0$ molar ratios of the *x* wt % Pt/3DOM CZY samples decreased

DOI: 10.1021/cs501773h
ACS Catal. 2015, 5, 1781−1793

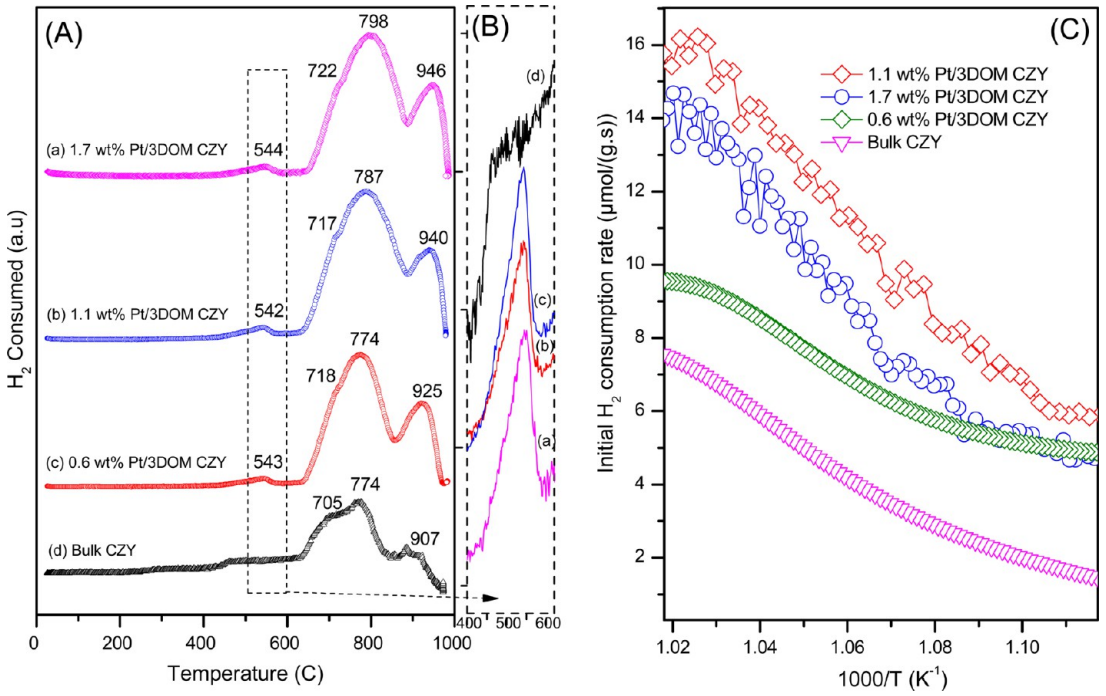

Figure 6. (A, B) H_2-TPR profiles of (a) 1.7 wt % Pt/3DOM CZY, (b) 1.1 wt % Pt/3DOM CZY, (c) 0.6 wt % Pt/3DOM CZY, and (d) Bulk CZY. (C) Initial H_2 consumption rate as a function of inverse temperature of *x* wt % Pt/3DOM CZY and Bulk CZY catalysts.

Table 3. Turnover Frequencies (TOF), Apparent Activation Energies (E_a), and Correlation Coefficients (R^2) of 3DOM CZY, Bulk CZY, and *x* wt % Pt/3DOM CZY Samples for Methane Combustion at Different Temperatures

	TOF_{Pt} (mol/(mol_{Pt} s))			TOF_{Ce} (mol/(mol_{Ce} s))			kinetic param[a]	
catalyst	300 °C	350 °C	400 °C	300 °C	350 °C	400 °C	E_a (kJ/mol)	R^2
3DOM CZY				2.42×10^{-8}	4.48×10^{-8}	9.07×10^{-8}	79	0.9990
0.6 wt % Pt/3DOM CZY	1.37×10^{-5}	4.19×10^{-5}	7.77×10^{-5}	1.11×10^{-7}	3.39×10^{-6}	6.28×10^{-6}	66	0.9991
1.1 wt % Pt/3DOM CZY	1.86×10^{-3}	3.68×10^{-3}	6.98×10^{-3}	5.01×10^{-7}	4.58×10^{-6}	2.25×10^{-5}	64	0.9992
1.7 wt % Pt/3DOM CZY	2.08×10^{-5}	3.18×10^{-5}	7.60×10^{-5}	3.56×10^{-7}	7.03×10^{-7}	1.33×10^{-6}	67	0.9996
Bulk CZY				1.22×10^{-7}	6.14×10^{-7}	8.65×10^{-7}	95	0.9992
1.2 wt % Pt/Bulk CZY	4.12×10^{-6}	4.62×10^{-7}	5.78×10^{-7}	5.97×10^{-9}	7.24×10^{-9}	8.01×10^{-10}	72	0.9993

[a]Reaction conditions: GHSV = 30000 mL/(g h) under the conditions of 2% CH_4 + 20% O_2 + 78% N_2 (balance) and total flow 41.6 mL/min.

with a rise in Pt loading: 0.52 for the 1.7 wt % Pt/3DOM CZY sample but 0.39 for the 0.6 wt % Pt/3DOM CZY sample. This result indicates that both metallic (in majority) and ionic (in minority) platinum species were present on the *x* wt % Pt/3DOM CZY samples. The cationic Pt ($Pt^{\delta+}$) species were considered to be more active than the metal state (Pt^0) species in oxidation reactions. Hence, the spectrum deconvolutions allow us to estimate the relative amount of each Pt species (Pt^0 and $Pt^{\delta+}$) on the surface of the *x* wt % Pt/3DOM CZY samples, and the results are presented in Table 2. After Pt loading, the rise in Ce^{3+} content of the *x* wt % Pt/3DOM CZY samples indicates that a strong interaction existed between Pt and CZY, a result due to the electron transfer from Pt^0 to Ce^{4+} in the CZY support. In other words, the Pt atoms ($Pt^0 \rightarrow Pt^{\delta+}$) could be oxidized by the surface Ce atoms ($Ce^{4+} \rightarrow Ce^{3+}$) even though there might be no direct Pt−Ce bonding. Furthermore, the changes in low-temperature reducibility shown below of the samples confirmed such a deduction.

3.6. Reducibility. H_2-TPR experiments were performed using 20 mg of the Bulk CZY or *x* wt % Pt/3DOM CZY samples, and their profiles are illustrated in Figure 6. As shown in Figure 6A, two reduction peaks at 774−798 and 907−946 °C were observed for the Bulk CZY and *x* wt % Pt/3DOM CZY samples. Since Y^{3+} and Zr^{4+} are both nonreducible under the H_2-TPR conditions adopted in the present investigation, the observed reduction peaks were due to the reduction of Ce^{n+} species.[13] The asymmetrical feature of either the low-temperature (<800 °C) or high-temperature (>800 °C) reduction peaks implies the existence of at least two kinds of Ce species at various coordination environments. Moreover, when Pt NPs were loaded on the 3DOM CZY surface, the low-temperature reduction peak at 774−798 °C was almost unchanged in position and shape, in comparison to that of the Pt-free 3DOM CZY sample (Figure 6B). The above XPS results (Figure 5B and Table 3) show that there still existed an appreciable quantity of $Pt^{\delta+}$ species on the surface of *x* wt % Pt/3DOM CZY and that modification of Pt NPs resulted in formation of a certain quantity of Ce^{4+}. Thus, the small peaks appeared at 543, 542, and 544 °C for the 0.6 wt % Pt/3DOM CZ, 1.1 wt % Pt/3DOM CZY, and 1.7 wt % Pt/3DOM CZY samples, respectively, which could be assigned to the reduction of $Pt^{\delta+}$ species. The first reduction peak at 774−798 °C of the *x* wt % Pt/3DOM CZY samples was due to a single-electron reduction of Ce^{3+} in the coordination-unsaturated microenvironments and/or due to the reduction of the chemically adsorbed oxygen species on the highly dispersed Pt NPs (i.e., from Pt−O_x to Pt)

DOI: 10.1021/cs501773h
ACS Catal. 2015, 5, 1781−1793

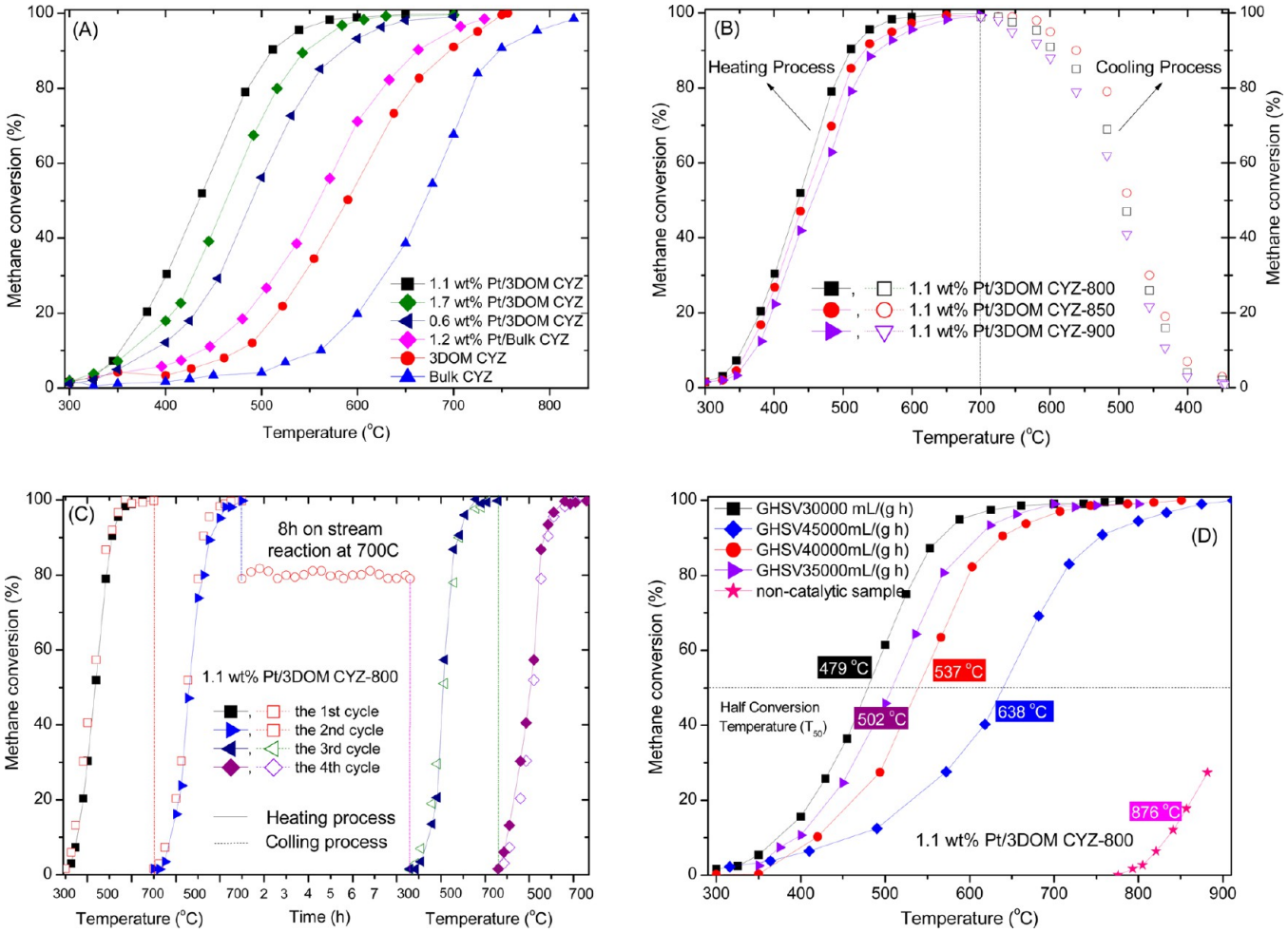

Figure 7. (A) Methane conversion versus temperature over the 3DOM CZY, *x* wt % Pt/3DOM CZY, and Bulk CZY catalysts. (B) Methane conversion versus temperature on different calcination. (C) Catalytic stability of the 1.1 wt % Pt/3DOM CZY catalyst. (D) Effect of GHSV on the catalytic activity over the 1.1 wt % Pt/3DOM CZY catalyst at GHSV = 30000 mL/(g h) under the conditions of 2% CH_4 + 20% O_2 + 78% N_2 (balance) and total flow of 41.6 mL/min.

or the interface between Pt NPs and CZY support (i.e., from Ce−O_x−Pt to Pt), which might be related to the weakening of the Ce−O bond induced by Pt atoms.[29,32] For the *x* wt % Pt/3DOM CZY and Bulk-CYZ samples, the total H_2 consumptions were in the range 13.7−14.5 and 18.0 mmol/g (Table 2 and Figure 6C), respectively. The reduction of CZY usually proceeds via the sequence $Ce^{4+} \rightarrow Ce^{3+}$. It has generally been accepted that the low-temperature reducibility of a catalyst can be conveniently evaluated using the initial (where less than 25% oxygen in the sample was removed for the first reduction peak) H_2 consumption rate.[35,36] Figure 6C shows the initial H_2 consumption rate as a function of inverse temperature of the Bulk CZY and *x* wt % Pt/3DOM CZY samples. It is clearly seen that the initial H_2 consumption rates of the samples increased in the order Bulk CZY < 0.6 wt % Pt/3DOM CZY < 1.7 wt % Pt/3DOM CZY < 1.1 wt % Pt/3DOM CZY. This changing trend in low-temperature reducibility was in good agreement with that in catalytic performance (shown below). These results suggest that there was the presence of morphology-dependent reducibility for the *x* wt % Pt/3DOM CZY samples, which was in good accordance with the results reported in the literature.[47]

3.7. Catalytic Performance. In the blank experiment (only quartz sands were loaded in the microreactor), we did not detect a significant conversion of CH_4 below 876 °C. This result demonstrates that no homogeneous reactions took place below 876 °C. Figure 7 shows the catalytic performances of the Bulk CZY, 3DOM CZY, and *x* wt % Pt/3DOM CZY samples for the combustion of CH_4 in the temperature range 300−900 °C under the conditions of 2 vol % CH_4 + 20 vol % O_2 + 78 vol % N_2 (balance) and GHSV of 30000 mL/(g h). It can be clearly observed from Figure 7 and Table 2 that the *x* wt % Pt/3DOM CZY and 1.2 wt % Pt/Bulk CZY samples performed much better than the 3DOM CZY and Bulk CZY samples. This result suggests that formation of macro-/mesoporous CZY was beneficial for enhancement in catalytic performance of the sample for CH_4 combustion. Preparing the macro-/mesoporous CZY with a high surface area and large pore volume could lead to excellent performance of the catalyst. The catalytic activity decreased at elevated GHSV values. At GHSV = 30000 mL/(g h) over the 1.1 wt % Pt/3DOM CZY sample, the $T_{50\%}$ and $T_{90\%}$ values were 479 and 598 °C (Figure 7D), respectively, which were 58 and 159 °C lower than those achieved at GHSV = 40000 mL/(g h). A further rise in GHSV from 40000 to 45000 mL/(g h) resulted in a drop in activity (Figure 7B). A further rise in calcination temperature from 850 to 900 °C caused a drop in activity. It is worth noting that the 1.7 wt % Pt/3DOM CZY sample showed an activity much inferior to

DOI: 10.1021/cs501773h
ACS Catal. 2015, 5, 1781−1793

that of 1.1 wt % Pt/3DOM CZY for methane oxidation, which might be due to the larger sizes of Pt NPs in the former in comparison to those in the latter, as confirmed by our HRTEM images (Figure 3h,m,r) of the samples. This result suggests that Pt NPs were the active sites for the combustion of CH_4 and the catalytic activity was related to the particle size and loading of Pt NPs.[48] It can be seen from Table 2 that the catalytic performance decreased in the sequence 1.1 wt % Pt/3DOM CZY > 1.7 wt % Pt/3DOM CZY > 0.6 wt % Pt/3DOM CZY > 1.2 wt % Pt/Bulk CZY > 3DOM CZY > Bulk CZY (Figure 7A), coinciding with the order in low-temperature reducibility (i.e., the initial H_2 consumption rate of the samples). Obviously, the 1.1 wt % Pt/3DOM CZY sample with a surface area of 84 m^2/g performed the best, giving $T_{10\%}$, $T_{50\%}$, and $T_{90\%}$ values of 385, 434, and 598 °C, respectively, which were much lower than those ($T_{10\%}$ = 476 °C, $T_{50\%}$ = 671 °C, and $T_{90\%}$ = 698 °C) achieved over the Bulk CZY sample with a surface area of 69 m^2/g by 113, 182, and 155 °C, respectively.

According to the activity data and moles of Ce in the CZY and *x* wt % Pt/3DOM CZY samples, we calculated the turnover frequencies (TOF_{Pt} (mol/(mol_{Pt} s)) and TOF_{Ce} (mol/(mol_{Ce} s)) and reaction rates (μmol/(g s)) from the number of CH_4 molecules converted by a single surface Pt site per second, the moles of Ce, and the Pt weight percentage in the *x* wt % Pt/3DOM CZY samples, respectively. The dispersion of platinum was estimated according to the reported procedure[32] and the assumption that Pt NPs displayed a spherical or hemispherical shape (as confirmed by the HRTEM images (Figures S8 and S9 in the Supporting Information) of the samples. The TOF_{Pt} and TOF_{Ce} values of the samples were calculated under the conditions of CH_4/O_2 molar ratio 1/10, GHSV = 30000 mL/(g h), and temperature 300, 350, and 400 °C, as summarized in Table 3. It is observed that, in comparison to the nonporous Bulk CZY sample at the same temperature, the TOF_{Ce} value (5.01×10^{-7} mol/(mol_{Ce} s)) of 1.1 wt % Pt/3DOM CZY was approximately 4.1 times that (1.22×10^{-7} mol/(mol_{Ce} s)) of Bulk CZY for methane combustion at 300 °C. With a rise in Pt loading from 0.6 to 1.1 wt %, the obtained 0.6 wt % Pt/3DOM CZY and 1.1 wt % Pt/3DOM CZY samples exhibited TOF_{Ce} values of 1.11×10^{-7} and 5.01×10^{-7} mol/(mol_{Ce} s) at 300 °C and 3.39×10^{-6} and 4.58×10^{-6} mol/(mol_{Ce} s) at 350 °C, respectively, but they decreased to 3.56×10^{-7} mol/(mol_{Ce} s) at 300 °C and 1.33×10^{-6} mol/(mol_{Ce} s) at 400 °C with a further rise in Pt loading from 1.1 to 1.7 wt %. In the meantime, one can also observe from Table 3 that the TOF_{Pt} values (1.86×10^{-3} mol/(mol_{Pt} s) at 300 °C and 6.98×10^{-3} mol/(mol_{Pt} s) at 400 °C) of the 1.1 wt % Pt/3DOM CZY sample were much higher than those (2.08×10^{-5} mol/(mol_{Pt} s) at 300 °C and 7.60×10^{-5} mol/(mol_{Pt} s) at 400 °C) of the 1.7 wt % Pt/3DOM CZY sample. It is clearly seen that the E_a values (95 and 79 kJ/mol, respectively) of the Bulk CZY and 3DOM CZY samples were much higher than those (64–67 kJ/mol) of the *x* wt % Pt/3DOM CZY samples (Table 3).

This result indicates that there was a strong SMSI between Pt NPs and CZY, which gave rise to an enhanced catalytic performance of *x* wt % Pt/3DOM CZY for methane combustion. In the past few years, the oxidation of methane and volatile organic compounds has been studied over various catalysts, as summarized in Table S2 in the Supporting Information. It is worth pointing out that, under similar reaction conditions, the catalytic activity ($T_{50\%}$ = 434 °C and $T_{90\%}$ = 598 °C) over our best-performing 1.1 wt % Pt/3DOM CZY sample was much better than those over $La_{0.9}Cu_{0.1}MnO_3$,[49] 20 wt % $LaMnO_3/MgO$,[50] $La_{0.5}Sr_{0.5}MnO_3$,[51] and La_2CuO_4 nanorods[52] but inferior to that over 1 wt % Pd/ZrO_2.[53] In addition, the catalytic stability of the 1.1 wt % Pt/3DOM CZY sample was tested in a consecutive reaction experiment (Figure 7C), in which the sample experienced first two runs of catalytic tests, then 8 h of on-stream reaction at 700 °C and 30000 mL/(g h), and finally two runs of catalytic tests. Each run lasted about 6 h. The overall test time was ca. 32 h. The result reveals that no obvious loss in activity was detected within 32 h of reaction.

3.8. Effects of Water Vapor and Sulfur Dioxide. Similar to the case for most of the oxide catalysts, cerium-based mixed oxide is also expected to be sensitive to sulfur poisoning. In fact, due to the basic properties of Ce and its substituents, cerium-based mixed oxides would thermodynamically show even higher sensitivity than the other transition-metal oxides. Nevertheless, poisoning seems to be primarily controlled by kinetics. It has been shown that sulfur dioxide could promote methane oxidation over the alumina-supported platinum[54] and ceria-supported platinum catalysts.[55] Thus, important variations in the rate of poisoning might occur, depending upon the composition and reaction conditions in the cases of Pt supported on ceria, silica, and alumina.[56] However, the Pt/$Ce_{1-x}Zr_xO_2$ catalyst has been shown to be relatively resistant to low sulfur concentrations.[57] The effect of moisture and SO_2 on the catalytic performance of the 1.1 wt % Pt/3DOM CZY sample for methane oxidation was examined, and the results are shown in Figure 8. Water-vapor-containing feed gas was introduced into the catalyst bed at temperatures of 550, 600, and 650 °C for 1 h, and then water-free feed gas was fed for 1 h. This alternating cycle was repeated four times. When the catalytic oxidation of CH_4 at 600 °C over the 1.1 wt % Pt/3DOM CZY sample became steady, 1.0, 3.0, or 5.0 vol % water vapor or 40 ppm of SO_2 in the feedstock was introduced to the reaction system. Methane conversion after on-stream reaction at 550 °C for 10 h was 66.5%, which was lower than that (76.5%) after on-stream reaction at 550 °C for 10 min. When 3.0 vol % water vapor was cut off, CH_4 conversion over 1.1 wt % Pt/3DOM CZY was almost restored to its initial value in the absence of H_2O. The addition of 3.0 vol % water vapor did not affect the catalytic activity of 1.1 wt % Pt/3DOM CZY if the reaction temperature was above 600 °C, but a decrease in activity occurred when the reaction temperature was below 550 °C (Figure 8A). Meanwhile, the catalytic activity was not significantly affected at a lower water vapor concentration (1.0 vol %), whereas introduction of a higher water vapor concentration (5.0 vol %) decreased the $T_{90\%}$ value by ca. 12% (Figure S11 in the Supporting Information). Furthermore, HRSEM images (Figure S12 in the Supporting Information) of the used 0.6 and 1.7 wt % Pt/3DOM CZY samples in the case of 3.0 vol % water vapor addition were rather similar to those of the fresh samples, and the surface area (80 m^2/g) of the used 1.1 wt % Pt/3DOM CZY sample was close to that (84 m^2/g) of the fresh counterpart. It is concluded that the presence of extra water vapor had more or less effect on the metal oxide support, rather than on the precious metal.[32,35] This might be due to the competitive adsorption of water and methane as well as oxygen molecules on the surface of 1.1 wt % Pt/3DOM CZY, where the adsorption of water was stronger than that of oxygen.

In order to examine the effect of SO_2 on the catalytic activity of the 1.1 wt % Pt/3DOM CZY sample, we carried out CH_4 oxidation in the presence of 40 ppm of SO_2 in the feedstock

DOI: 10.1021/cs501773h
ACS Catal. 2015, 5, 1781–1793

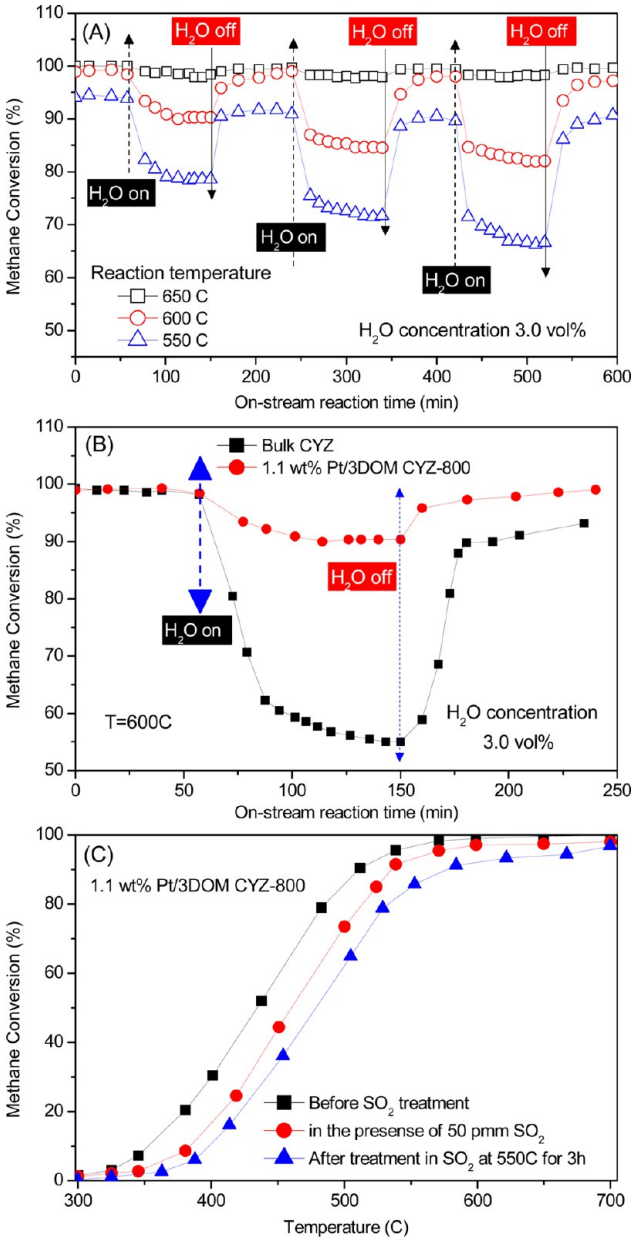

Figure 8. (A) Effect of water vapor on methane conversion at different reaction temperatures over the 1.1 wt % Pt/3DOM CZY catalyst (H_2O concentration 3.0 vol %). (B) Effect of water introduction or cutting off in the feedstock over 1.1 wt % Pt/3DOM CZY and Bulk CZY at 600 °C (H_2O concentration 3.0 vol %). (C) Effect of SO_2 on methane conversion over the 1.1 wt % Pt/3DOM CZY catalyst under the conditions of GHSV = 30000 mL/(g h) and SO_2 concentration 40 ppm.

and then switched the SO_2-containing atmosphere to an SO_2-free atmosphere at 550 °C (Figure 8C). No significant deactivation due to SO_2 introduction was observed. After this sample was treated in 40 ppm of SO_2 at 550 °C for 3 h, the catalytic activity decreased by ca. 5%. This result indicates that the 1.1 wt % Pt/3DOM CZY sample was highly resistant to SO_2 poisoning. According to the results of the present investigation and those reported previously,[35,58] we believe that platinum could also improve the resistance to sulfur poisoning, mainly by increasing the concentration of acidic Ce^{4+} ions and weakening the SO_2 adsorption on the sample. Furthermore, the HRSEM images (Figures S12 and S13 in the Supporting Information) of the used 0.6 wt % Pt/3DOM CZY sample reveal that the Pt NPs were well stabilized on the surface of 3DOM CZY after 30 h of on-stream reaction in the presence of 3.0 vol % H_2O (Figure S14 in the Supporting Information). These results show that the *x* wt % Pt/3DOM CZY samples were catalytically stable in the case of introduction of water vapor or SO_2 at a lower concentration.

3.9. Apparent Activation Energy. In the past few years, there have been reports on the kinetic behaviors of methane combustion in the literature. For instance, Landi et al. observed that the combustion kinetics of CH_4, H_2, and CO over a $LaMnO_3$-based catalyst was proven to be first order toward methane concentration and zero order toward oxygen concentration.[59] Chen et al. claimed that the oxidation of CH_2Cl_2 over Au/Co_3O_4 was first order toward CH_2Cl_2 concentration and zero order toward oxygen concentration.[60] Deng et al. pointed out that methanol oxidation over Au/Al_2O_3 was first order toward methanol concentration and zero order toward oxygen concentration.[61] Good linear Arrhenius plots were obtained over the supported Ag NPs catalysts for methane oxidation when the reaction was first order toward methane concentration.[36,58] Therefore, it is reasonable to suppose that the combustion of methane in the presence of excess oxygen (CH_4/O_2 molar ratio 1/10) would obey a first-order reaction mechanism with respect to methane concentration: $r = -kc = (-A \exp(-E_a/RT))c$, where *r*, *k*, *A*, and E_a are the reaction rate (μmol/(g s)), rate constant (s^{-1}), pre-exponential factor, and apparent activation energy (kJ/mol), respectively. Figure 9 shows the Arrhenius plots for methane combustion at a CH_4 conversion of <20% (at which the temperature range was 300−550 °C) over the Bulk CZY, 3DOM CZY, and *x* wt % Pt/3DOM CZY samples. According to the slopes of the linear (correlation coefficients (R^2) were above 0.99) Arrhenius plots, one can calculate the *k* and E_a values for CH_4 combustion over these samples, as summarized in Table 3. It can be observed that the E_a value decreased in the sequence Bulk CZY > 3DOM CZY > 1.7 wt % Pt/3DOM CZY > 0.6 wt % Pt/3DOM CZY > 1.1 wt % Pt/3DOM CZY, with the lowest E_a value (64.7−67.1 kJ/mol) being achieved over the *x* wt % Pt/3DOM CZY samples. This result suggests that methane oxidation might proceed more readily over the macro-/mesoporous CZY-supported Pt samples. The great discrepancy in E_a might be related to the difference in the total number of active sites and the presence of a strong Pt−CZY interaction. As we know, the presence of a 3DOM network within the CZY sample allows better diffusion of the reactants (CH_4 and O_2), hence leading to easy accessibility of active sites for the reactant molecules. This could consequently increase the oxidation rates of reactants, and catalytic performance would be improved as a result. The oxidation of methane over *x* wt % Pt/3DOM CZY could proceed via a suprafacial mechanism. After Pt loading, partial Ce^{4+} species were reduced to Ce^{3+} species by Pt^0 via the strong SMSI between Pt NPs and CZY, resulting in the formation of surface oxygen vacancies. The gas-phase O_2 molecules were then activated in the oxygen vacancies near the Pt−CZY interface to active oxygen species. On the other hand, loading of Pt NPs could significantly promote the adsorption of CH_4, enhancing the migration of chemisorbed methane to the Pt−CZY interface. Hence, methane oxidation could occur between the chemisorbed CH_4 and active oxygen species at the Pt−CZY interface. As can be seen from Table 3, the apparent activation energy (64 kJ/mol) obtained over 1.1 wt % Pt/3DOM CZY was close to or slightly lower than those (73−89 kJ/mol) over

DOI: 10.1021/cs501773h
ACS Catal. 2015, 5, 1781−1793

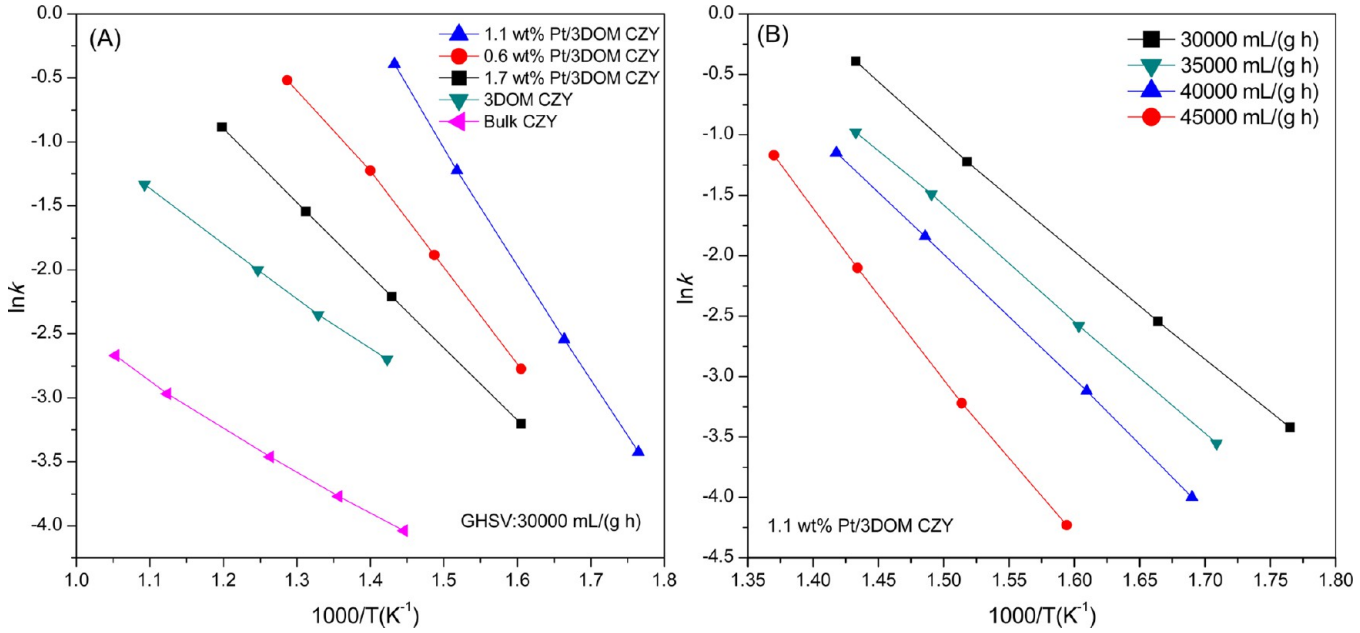

Figure 9. Arrhenius plots for methane combustion over (A) Bulk CZY, 3DOM CZY, 1.1 wt % Pt/3DOM CZY samples at GHSV = 30000 mL/(g h) and (B) 1.1 wt % Pt/3DOM CZY at different GHSV values.

$M_xFe_{3-x}O_4$ (M = Ni, Mn; x = 0.50−0.65)[62] and that (67 kJ/mol) over $Pt/Ce_{0.64}Zr_{0.15}Bi_{0.21}O_{1.895}/Al_2O_3$[63] and much lower than those (120−144 kJ/mol) over CuO/Al_2O_3 and MnO/Al_2O_3.[64] Therefore, the results of kinetic investigations confirm that the x wt % Pt/3DOM CZY samples showed excellent catalytic performance for the combustion of methane. We believe that such a material will be promising in practical applications for methane combustion.

4. CONCLUSIONS

In conclusion, we have demonstrated a facile synthesis of 3DOM CZY with mesoporous walls and high surface areas (84−95 m^2/g) and x wt % Pt/3DOM CZY with high dispersion of ultrafine Pt NPs by the gas-bubbling CTAB/P123-assisted reduction method. The x wt % Pt/3DOM CZY possessed a well-defined interconnected macroporous structure with a two-dimensional aligned mesopore size of 3.5−4.6 nm, an interconnected macropore wall thickness of 13−19 nm, and a mean Pt particle size of 2.6−4.2 nm. There were good correlations of O_{ads} concentration and low-temperature reducibility with catalytic activity of the sample for the oxidation of CH_4. The 1.1 wt % Pt/3DOM CZY sample showed the best catalytic performance ($T_{90\%}$ = 598 °C), and the apparent activation energy (E_a = 64 kJ/mol) over 1.1 wt % Pt/3DOM CZY was the lowest. The addition of 3.0 vol % water vapor did not affect the catalytic activity of 1.1 wt % Pt/3DOM CZY at temperatures above 600 °C, but it decreased the catalytic activity at temperatures below 550 °C. There was a small negative effect of SO_2 on the catalytic activity of 1.1 wt % Pt/3DOM CZY. We believe that the high catalytic performance of 1.1 wt % Pt/3DOM CZY for methane combustion might be attributed to its large surface area, high oxygen adspecies concentration, good low-temperature reducibility, unique 3DOM structure, and strong interaction between Pt NPs and 3DOM CZY.

■ ASSOCIATED CONTENT

Supporting Information

The following file is available free of charge on the ACS Publications website at DOI: 10.1021/cs501773h.

Catalyst characterization procedures, synthesis of monodispersive PMMA microspheres, catalytic activity measurements, SEM images of PMMA microspheres, HRTEM/HRSEM images of 3DOM CZY support and x wt % Pt/3DOM CZY catalysts, XPS spectra of the samples, HRSEM images of 0.6 wt % Pt/3DOM CZY and 1.7 wt % Pt/3DOM CZY samples after 30 h on stream, effects of water vapor concentration over 1.1 wt % Pt/3DOM CZY, and on-stream methane combustion activity of 1.7 wt % Pt/3DOM CZY (PDF)

■ AUTHOR INFORMATION

Corresponding Authors

*H.A.: e-mail, h.arandiyan@unsw.edu.au; tel, +61-2-9385 7994.
*H.D.: e-mail, hxdai@bjut.edu.cn; tel, +86-10-6739 6118.
*J.L.: e-mail, lijunhua@tsinghua.edu.cn; tel, +86-10-6277 1093.

Notes

The authors declare no competing financial interest.

■ ACKNOWLEDGMENTS

The authors acknowledge financial support from the National Natural Science Fund of China (Grant Nos. 21221004, 21077007, and 21377008), National High-Tech Research Development (863) Program of China (Grant No. 2013AA065304), Foundation on the Creative Research Team Construction Promotion Project of Beijing Municipal Institutions, and Scientific Research Base Construction−Science and Technology Creation Platform−National Materials Research Base Construction.

■ REFERENCES

(1) Eguchi, K.; Arai, H. *Catal. Today* **1996**, *29*, 379−386.

DOI: 10.1021/cs501773h
ACS Catal. 2015, 5, 1781−1793

(2) Centi, G.; Ciambelli, P.; Perathoner, S.; Russo, P. *Catal. Today* **2002**, *75*, 3−15.
(3) Zwinkels, M. F. M.; Järås, S. G.; Menon, P. G.; Griffin, T. A. *Catal. Rev. Sci. Eng.* **1993**, *35*, 319−358.
(4) Kirchnerova, J.; Klvana, D. *Catal. Lett.* **2000**, *67*, 175−181.
(5) Eltejaei, H.; Reza Bozorgzadeh, H.; Towfighi, J.; Reza Omidkhah, M.; Rezaei, M.; Zanganeh, R.; Zamaniyan, A.; Zarrin Ghalam, A. *Int. J. Hydrogen Energy* **2012**, *37*, 4107−4118.
(6) Liu, J.; Zhao, Z.; Wang, J.; Xu, C.; Duan, A.; Jiang, G.; Yang, Q. *Appl. Catal., B* **2008**, *84*, 185−195.
(7) Zhang, G.; Zhao, Z.; Xu, J.; Zheng, J.; Liu, J.; Jiang, G.; Duan, A.; He, H. *Appl. Catal., B* **2011**, *107*, 302−315.
(8) Bai, B.; Arandiyan, H.; Li, J. *Appl. Catal., B* **2013**, *142−143*, 677−683.
(9) Liu, J.; Zhao, Z.; Lan, J.; Xu, C.; Duan, A.; Jiang, G.; Wang, X.; He, H. *J. Phys. Chem. C* **2009**, *113*, 17114−17123.
(10) Fornasiero, P.; Balducci, G.; Di Monte, R.; Kašpar, J.; Sergo, V.; Gubitosa, G.; Ferrero, A.; Graziani, M. *J. Catal.* **1996**, *164*, 173−183.
(11) Trovarelli, A.; Zamar, F.; Llorca, J.; Leitenburg, C. D.; Dolcetti, G.; Kiss, J. T. *J. Catal.* **1997**, *169*, 490−502.
(12) Madier, Y.; Descorme, C.; Le Govic, A. M.; Duprez, D. *J. Phys. Chem. B* **1999**, *103*, 10999−11006.
(13) He, H.; Dai, H. X.; Ng, L. H.; Wong, K. W.; Au, C. T. *J. Catal.* **2002**, *206*, 1−13.
(14) Zhang, Y.; Zhang, L.; Deng, J.; Dai, H.; He, H. *Inorg. Chem.* **2009**, *48*, 2181−2192.
(15) Wang, G.; Dai, H.; Zhang, L.; Deng, J.; Liu, C.; He, H.; Au, C. T. *Appl. Catal., A* **2010**, *375*, 272−278.
(16) Nishihata, Y.; Mizuki, J.; Akao, T.; Tanaka, H.; Uenishi, M.; Kimura, M.; Okamoto, T.; Hamada, N. *Nature* **2002**, *418*, 164−167.
(17) Arandiyan, H. R.; Parvari, M. *Braz. J. Chem. Eng.* **2009**, *26*, 63−74.
(18) Arandiyan, H. R.; Parvari, M. *J. Nat. Gas Chem.* **2008**, *17*, 213−224.
(19) Arandiyan, H.; Chang, H.; Liu, C.; Peng, Y.; Li, J. *J. Mol. Catal., A* **2013**, *378*, 299−306.
(20) Arandiyan, H.; Peng, Y.; Liu, C.; Chang, H.; Li, J. *J. Chem. Technol. Biotechnol.* **2014**, *89*, 372−381.
(21) Hadian, N.; Rezaei, M. *Fuel* **2013**, *113*, 571−579.
(22) Sadakane, M.; Horiuchi, T.; Kato, N.; Sasaki, K.; Ueda, W. *J. Solid State Chem.* **2010**, *183*, 1365−1371.
(23) Hara, M.; Nakano, H.; Dokko, K.; Okuda, S.; Kaeriyama, A.; Kanamura, K. *J. Power Sources* **2009**, *189*, 485−489.
(24) Wei, Y.; Zhao, Z.; Li, T.; Liu, J.; Duan, A.; Jiang, G. *Appl. Catal., B* **2013**, *146*, 57−70.
(25) Xie, S.; Deng, J.; Zang, S.; Yang, H.; Guo, G.; Arandiyan, H.; Dai, H. *J. Catal.* **2015**, *322*, 38−48.
(26) Wei, Y.; Liu, J.; Zhao, Z.; Duan, A.; Jiang, G.; Xu, C.; Gao, J.; He, H.; Wang, X. *Energy Environ. Sci.* **2011**, *4*, 2959−2970.
(27) Li, X.; Dai, H.; Deng, J.; Liu, Y.; Zhao, Z.; Wang, Y.; Yang, H.; Au, C. T. *Appl. Catal., B* **2013**, *458*, 11−20.
(28) Wang, Y.; Dai, H.; Deng, J.; Liu, Y.; Arandiyan, H.; Li, X.; Gao, B.; Xie, S. *Solid State Sci.* **2013**, *24*, 62−70.
(29) Wang, Y.; Dai, H.; Deng, J.; Liu, Y.; Zhao, Z.; Li, X.; Arandiyan, H. *Chem. Eng. J.* **2013**, *226*, 87−94.
(30) Xie, S.; Dai, H.; Deng, J.; Yang, H.; Han, W.; Arandiyan, H.; Guo, G. *J. Hazard. Mater.* **2014**, *279*, 392−401.
(31) Li, X.; Dai, H.; Deng, J.; Liu, Y.; Xie, S.; Zhao, Z.; Wang, Y.; Guo, G.; Arandiyan, H. *Chem. Eng. J.* **2013**, *228*, 965−975.
(32) Liu, Y.; Dai, H.; Deng, J.; Li, X.; Wang, Y.; Arandiyan, H.; Xie, S.; Yang, H.; Guo, G. *J. Catal.* **2013**, *305*, 146−153.
(33) Ji, K.; Deng, J.; Zang, H.; Han, J.; Arandiyan, H.; Dai, H. *Appl. Catal., B* **2015**, *165*, 285−295.
(34) Ji, K.; Dai, H.; Deng, J.; Zang, H.; Arandiyan, H.; Xie, S.; Yang, H. *Appl. Catal., B* **2015**, *168*, 274−282.
(35) Arandiyan, H.; Dai, H.; Deng, J.; Liu, Y.; Bai, B.; Wang, Y.; Li, X.; Xie, S.; Li, J. *J. Catal.* **2013**, *307*, 327−339.
(36) Arandiyan, H.; Dai, H.; Deng, J.; Wang, Y.; Xie, S.; Li, J. *Chem. Commun.* **2013**, *49*, 10748−10750.
(37) Tan, W.; Guo, G.; Deng, J.; Xie, S.; Yang, H.; Jiang, Y.; Dai, H. *Ind. Eng. Chem. Res.* **2014**, *53*, 18452−18461.
(38) Herzing, A. A.; Kiely, C. J.; Carley, A. F.; Landon, P.; Hutchings, G. J. *Science* **2008**, *321*, 1331−1335.
(39) Fang, P.; Luo, M.-F.; Lu, J.-Q.; Cen, S.-Q.; Yan, X.-Y.; Wang, X.-X. *Thermochim. Acta* **2008**, *478*, 45−50.
(40) Sakai, N.; Yamaji, K.; Xiong, Y. P.; Kishimoto, H.; Horita, T.; Yokokawa, H. *J. Electroceram.* **2004**, *13*, 677−682.
(41) Sun, Y.; Xia, Y. *Adv. Mater.* **2002**, *14*, 833−837.
(42) Burroughs, P.; Hamnett, A.; Orchard, A. F.; Thornton, G. *J. Chem. Soc., Dalton Trans.* **1976**, 1686−1698.
(43) Wang, G.; Zhang, L.; Dai, H.; Deng, J.; Liu, C.; He, H.; Au, C. T. *Inorg. Chem.* **2008**, *47*, 4015−4022.
(44) Buscaglia, M. T.; Buscaglia, V.; Bottino, C.; Viviani, M.; Fournier, R.; Sennour, M.; Presto, S.; Marazza, R.; Nanni, P. *Cryst. Growth Des.* **2008**, *8*, 3847−3855.
(45) Mitsuyasu, H.; Nonaka, Y.; Eguchi, K.; Arai, H. *J. Solid State Chem.* **1997**, *129*, 74−81.
(46) Di Monte, R.; Kašpar, J. *J. Mater. Chem.* **2005**, *15*, 633−648.
(47) Zhiqiang, Y.; Kebin, Z.; Xiangwen, L.; Qun, T.; Deyi, L.; Sen, Y. *Nanotechnology* **2007**, *18*, 185606−185609.
(48) Fouladvand, S.; Skoglundh, M.; Carlsson, P.-A. *Catal. Sci. Technol.* **2014**, *4*, 3463−3473.
(49) Bulgan, G.; Teng, F.; Liang, S. H.; Yao, W. Q.; Zhu, Y. F. *Wuli Huaxue Xuebao/Acta Physico − Chimica Sinica* **2007**, *23*, 1387−1392.
(50) Svensson, E. E.; Nassos, S.; Boutonnet, M.; Järås, S. G. *Catal. Today* **2006**, *117*, 484−490.
(51) Sun, X.; Lin, J. *J. Phys. Chem. C* **2009**, *113*, 4970−4975.
(52) Zhang, L.; Zhang, Y.; Dai, H.; Deng, J.; Wei, L.; He, H. *Catal. Today* **2010**, *153*, 143−149.
(53) Araya, P.; Guerrero, S.; Robertson, J.; Gracia, F. J. *Appl. Catal., A* **2005**, *283*, 225−233.
(54) Corro, G.; Cano, C.; Garcia Fierro, J. L. *Catal. Commun.* **2008**, *9*, 2601−2605.
(55) Kylhammar, L.; Carlsson, P.-A.; Skoglundh, M. *J. Catal.* **2011**, *284*, 50−59.
(56) Bounechada, D.; Fouladvand, S.; Kylhammar, L.; Pingel, T.; Olsson, E.; Skoglundh, M.; Gustafson, J.; Di Michiel, M.; Newton, M. A.; Carlsson, P.-A. *Phys. Chem. Chem. Phys.* **2013**, *15*, 8648−8661.
(57) Zhang, L.; Weng, D.; Wang, B.; Wu, X. *Catal. Commun.* **2010**, *11*, 1229−1232.
(58) Arandiyan, H.; Dai, H.; Deng, J.; Wang, Y.; Sun, H.; Xie, S.; Bai, B.; Liu, Y.; Ji, K.; Li, J. *J. Phys. Chem. C* **2014**, *118*, 14913−14928.
(59) Landi, G.; Barbato, P. S.; Di Benedetto, A.; Pirone, R.; Russo, G. *Appl. Catal., B* **2013**, *134−135*, 110−122.
(60) Chen, B.; Bai, C.; Cook, R.; Wright, J.; Wang, C. *Catal. Today* **1996**, *30*, 15−20.
(61) Deng, Q.; Li, X.-M.; Peng, Z.-S.; Long, Y.-F.; Xiang, L.-M.; Cai, T.-J. *Trans. Nonferrous Met. Soc. China* **2010**, *20*, 437−442.
(62) Florea, M.; Alifanti, M.; Parvulescu, V. I.; Mihaila-Tarabasanu, D.; Diamandescu, L.; Feder, M.; Negrila, C.; Frunza, L. *Catal. Today* **2009**, *141*, 361−366.
(63) Masui, T.; Imadzu, H.; Matsuyama, N.; Imanaka, N. *J. Hazard. Mater.* **2010**, *176*, 1106−1109.
(64) Saqer, S. M.; Kondarides, D. I.; Verykios, X. E. *Appl. Catal., B* **2011**, *103*, 275−286.

DOI: 10.1021/cs501773h
ACS Catal. 2015, 5, 1781−1793